ELECTRONIC SEISMOLOGIST

Fitting Waveform Envelopes to Derive Focal Mechanisms of Moderate Earthquakes

by Jiří Zahradník and Efthimios Sokos

ABSTRACT

Focal mechanisms of shallow crustal earthquakes with magnitude 4 or less remain unresolved in many regions of the world due to the sparseness of seismic networks. Relatively distant stations must be used, but modeling those waveforms is difficult due to imprecision of seismic-velocity models. The waveform inversions also suffer from instrumental problems, such as flipped channel sign and errors in gain or timing. In such situations, waveforms should therefore be substituted by a robust characteristic which still carries information about focal mechanism and moment magnitude. We propose inversion of waveform envelopes. Three application examples demonstrate the performance of the method for earthquakes in various ranges of epicentral distance and frequency. In the examples, the focal mechanisms of the sample earthquakes are known from the waveform inversion approach based on near-source stations. The near-source stations are then ignored completely. Use of the remaining stations fails to provide the true mechanism through waveform inversion, but a correct estimate of the solution is found using envelopes. This method may be of interest to seismologists who need to compute focal mechanisms for stress-field studies in sparse networks, where traditional waveform inversion and amplitude inversion methods often fail.

Electronic Supplement: Figures and text illustrating robustness of envelopes relative to waveforms, problems when increasing frequency, importance of the posterior polarity constraint, and synthetic tests addressing the effects of noise and imprecise velocity models.

INTRODUCTION AND MOTIVATION

Huge regions of the globe are still in need of detailed geophysical analyses of stress field and seismogenic potential of faults. A limiting factor is the absence of focal mechanisms and moment magnitudes for small earthquakes, which is basically caused by the sparseness of existing seismic networks and limited availability of detailed structural models. We propose the inversion of waveform envelopes, implemented as a new tool in the widely used ISOLA software.

Imperfect velocity models are a nightmare for analysts who, for various reasons, need to calculate focal mechanisms of moderate earthquakes at relatively distant stations where low-frequency signals are hidden in the noise. This problem has been solved by inverting focal mechanisms simultaneously with time shifts or by including the timing and amplitude corrections from calibration events (Tan and Helmberger, 2007). Other researchers invert their data (e.g., dispersion curves) first into *ad hoc* velocity models and then invert waveforms with the path-specific models (Dias *et al.*, 2016). Recently, using Bayesian approaches, assumed uncertainties of velocity models have been projected into uncertainties of the focal mechanisms (Wéber, 2006; Halló and Gallovič, 2016). The problem is even more challenging because station metadata information (e.g., amplification, polarity, sensor orientation, and time corrections) is not always available, correct, and/or complete. Therefore, robustness of the interpretation methods with respect to imperfect velocity models and to the aforementioned instrumental problems should be improved. Toward this goal, if the waveform inversion fails, we propose substituting waveforms by envelopes.

Why use envelopes? Although teleseismic backprojection of relatively simple waveforms is feasible, regional or local source scanning operates rather on envelopes (Baker *et al.*, 2005). Coda waves, employed in attenuation studies, are modeled with envelopes because of inherent complexity of scattered waves (Chouet, 1979). Pioneering simulations of strong ground motions were performed with random noise, properly windowed by presumed envelope shapes, because high-frequency motions contain a stochastic component (Boore, 1983). The idea of using envelopes of high-frequency records for focal mechanisms of low-magnitude events has been mentioned (Dahal and Ebel, 2016). Unmodeled waveform features in imperfect velocity models may call for similar simplification, even at low frequencies.

Intuitively, it is easy to understand the role of envelopes. For example, considering a band-pass signal $y(t)$ which looks like a single sine pulse of period T, an unmodeled time shift close to $T/2$ transforms this signal into $-y(t)$, but the envelope is still the same. Note a certain similarity between using envelopes and amplitude spectra (Zahradník *et al.*, 2001; Cesca *et al.*, 2010) that ignore unmodeled time shifts and sign

doi: 10.1785/0220170161

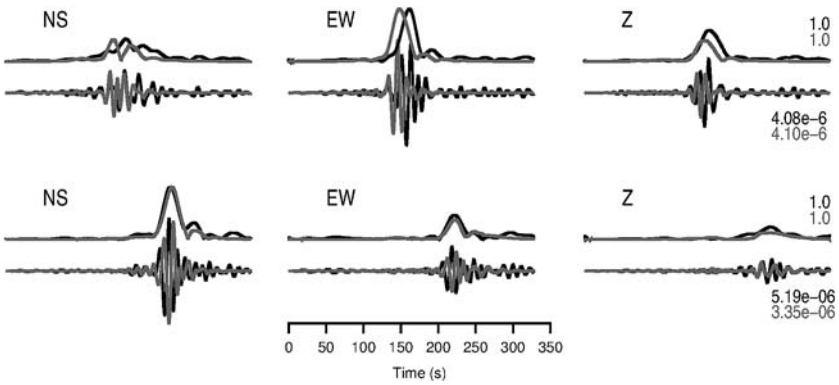

▲ **Figure 1.** Schematic example of waveforms and their normalized envelopes. Comparison between real data (black) and synthetics (gray) at two stations for which epicentral distance is ~12 and 20 wavelengths (top and bottom, respectively). Peak values are shown on the right. Note the significant waveform dissimilarities and envelope similarities.

reversals. It is worth reminding about the concept of envelope detectors of radio signals; considering the amplitude modulated signal $x(t) = e(t)\cos(\omega t + \varphi(t))$ and assuming that the phase component $\varphi(t)$ of the signal is uncertain and the carrier frequency ω is constant (or the band-pass signal is short), then all the information is fully characterized by the envelope $e(t)$. Hereafter, the term "envelope" in this article will mean just its shape; that is, $e(t)$ and $e(t+\tau)$ with an arbitrary time shift τ have the same envelopes. The concept of the time-independent shape of a complete waveform is a generalization of the time-independent amplitudes and amplitude ratios, for example, S/P (Hardebeck and Shearer, 2003), or transverse/radial (Vavryčuk and Kim, 2014).

For motivation, we start with a schematic example (Fig. 1). It comes from real-world data (an M_w 4.4 event), later discussed in Figure 2. At this moment, all specific parameters are unimportant; we just show a typical comparison between real and synthetic waveforms at epicentral distances that are relatively large with respect to the used wavelength (distances ~360 and 600 km at frequencies < 0.1 Hz are equivalent to ~12 and 20 minimum shear wavelengths [MSWs]). Synthetics are forward simulated using a reliable focal mechanism. Figure 1 demonstrates that real and synthetic data are dissimilar, featuring large time shifts up to ~15 s and amplitude ratios up to ~1.7. These dissimilarities are caused by the imprecision of the assumed velocity model, which becomes critical due to large epicentral distance. However, we also observe in Figure 1 that the shapes of real and synthetic normalized envelopes are similar, and both display almost the same relative strength of the components (i.e., the same ratio of N-to-E-to-Z). In this sense, the envelopes appear to be more robust with respect to velocity models than waveforms. The normalization makes the envelopes insensitive to errors in instrumental gain (assuming the same gain in all three components at any station) and also insensitive to errors in absolute time.

We developed a new method and present its application on three selected earthquakes to encourage wider use of the envelope-inversion technique. Each example has some specific feature making it problematic for waveform inversion but demonstrates the success of the envelope inversion. For example, for an M_w 4.4 event previously inverted from waveforms at favorably distributed near-source stations, we obtain a reliable reference solution. Then, we simulate a hypothetical case in which the near-source stations are missing, and only distant stations are available (~300–600 km); their waveform inversion fails, but the envelope inversion still provides a good estimate of the reference mechanism. Two additional similar thought experiments are presented, with M_w 3.4 and 2.9 events, demonstrating the usefulness of envelopes at 39–137 km and 5–46 km distance ranges, respectively.

METHOD

The method is designed to calculate a point-source pure double-couple (DC) source model. Real waveforms are instrument corrected to velocity. Stations and components are selected, and a station-dependent frequency range is defined. A fourth-order band-pass causal (i.e., a single-pass) Butterworth filter is applied, and the filtered waveforms are integrated to compute displacements. Then, real-data envelopes are calculated using the Hilbert transform. Full-wave Green's functions are calculated in a 1D velocity model, using the discrete wavenumber method, for a set of trial source positions. Green's functions are convolved with five elementary DC moment tensors, thus producing elementary seismograms. These are band-pass filtered in the same way as the real data and integrated into displacements.

The inversion of real envelopes consists of two nested loops, performing a grid search over the source position (e.g., several depths) and over the strike/dip/rake (s/d/r) angles, respectively. A synthetic seismogram for any assumed depth and s/d/r combination is obtained as a linear combination of the elementary seismograms; the synthetics are calculated for a unit seismic moment. The envelopes of synthetic seismograms are calculated in the same way as the envelopes of real waveforms, that is, using the same frequency band. As regards the s/d/r angles, the method allows two modes: with and without preconstraining the angles. In the nonconstrained mode, we search the whole parameter space (discretized typically with 10° steps for each angle, as will be the case throughout this article). In the preconstrained method, the code visits only s/d/r combinations previously checked for agreement with polarities (Fojtíková and Zahradník, 2014). If using the nonconstrained mode, the resulting focal mechanism must go through a posterior polarity check with at least one polarity, because envelopes do not resolve the 180° ambiguity of rake. Polarities can be prescribed also for the stations which do not participate in the envelope inversion. The grid search minimizes global misfit between real and synthetic envelopes, using the L2 norm and user-specified weights; zero weights can be used to remove

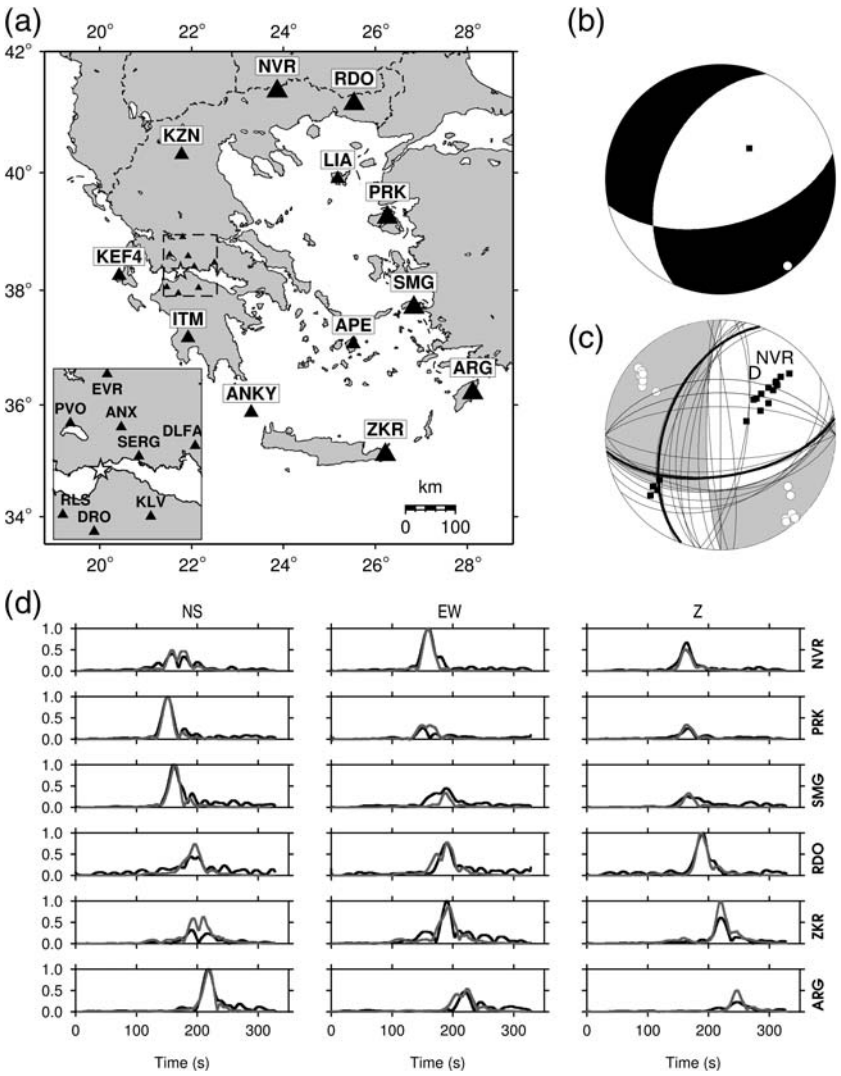

▲ **Figure 2.** Event A, M_w 4.4. (a) All stations considered in the inversion. For the eight near-source stations (27–67 km) used to calculate the reference solution, see the inset. An unfavorable subset of six distant stations (381–609 km), shown as large triangles, has been chosen to demonstrate the usefulness of the envelope inversion in the simulated absence of the near-source stations. A star shows the epicenter. (b) Reference focal mechanism solution from the near-source stations. (c) Envelope inversion proposed in this article, using the six unfavorable distant stations. The best-fitting envelope solution is shown by shading in (c). Nodal lines correspond to the solution ensemble constrained by a single-station polarity (NVR, D denotes down) and deviating from the minimum misfit by less than 10%. The ensemble consists of two families, one of them near the reference solution; the nearest solution is shown with bold lines. (d) Observed (black) and synthetic (gray) envelopes, 0.05–0.10 Hz, for the best-fitting solution; variance reduction (VR) = 0.82.

noisy components. The seismic moment is calculated for the best-fitting solution, and synthetic envelopes are then plotted together with the real ones.

Thanks to a systematic search of the parameter space, we obtain not only the best-fitting solution, but we also identify an ensemble of solutions that fit the data almost equally well, within a certain misfit threshold. The whole ensemble is important. It is because the true solution of the problem may differ from the best-fitting one, but the true solution should be encompassed within the ensemble. All nodal lines and P–T axes within the threshold are plotted on the focal sphere, together with observed first-motion polarities. A low/high threshold is equivalent to assuming a low/high data error, as explained in more detail at the end of this section.

The L2-norm misfit between real and synthetic envelopes is evaluated at their temporal shifts, which maximize lagged cross correlation; this is done individually for each component. Before the inversion, the observed envelopes (denoted O_i) are normalized individually at each station I; that is, they are divided by the largest absolute value at the station (Max O_i). Synthetic envelopes are also normalized (Max S_i) but repeatedly for every tested source position and s/d/r triplet. For the best-fitting solution, the observed and synthetic data are multiplied by the Max O_i and Max S_i values to renormalize them to their true values (O_i and S_i). Finally, the scalar seismic moment is calculated using equation (9) of Zahradník and Gallovič (2010): $M_0 = \sum w_i^2 O_i S_i / \sum w_i^2 S_i^2$, in which w_i are the weights previously used in the misfit minimization. Finally, M_0 is converted into moment magnitude (M_w).

It remains to explain how to choose a suitable misfit threshold. To that goal, assuming Gaussian data errors, we employ the Chi-square (χ^2) statistic. Let X be a sum of squares of n-independent Gaussian variables with zero mean and unit variance. In our problems, we consider $X = R/\sigma_d^2$, in which R is the sum of squared data residuals (observed minus synthetic, at all stations), and σ_d^2 is the data error variance. Then, X has a χ^2 distribution with n degrees of freedom for which the limit (when n is large) is a Gaussian distribution. The mean of this distribution is $E(X) = n$, and the variance $\sigma_X^2 = 2n$. In this article, we define a "one-sigma" relative tolerated range of X, or threshold: $\mathrm{Thr}[\%] = 100\,\Delta X/E(X) = 100\,\sigma_X/n = 100\sqrt{(2/n)}$. The number of degrees of freedom in the seismic data can be estimated, based on the uncertainty principle, as $n = 2\Delta T \Delta W$, in which ΔT and ΔW stand for the studied frequency and time range, respectively. The quantity $\Delta T \Delta W$ is the time-bandwidth product; in our problems, it typically equals ~10 per seismogram component. Hence, for N_{st} three-component stations, $n \sim 30 \times N_{st} \sim 100$–$1000$. Thus, we arrive at Thr ~ 14%–4%. For this reason, and because in practice we do not know the exact value of n, the grid-search inversions are inspected with several thresholds of this order of magnitude, for example,

Table 1
Hypocentral Parameters and Focal Mechanisms

Event	Date (yyyy/mm/dd)	Origin Time (hh:mm:ss.ss)	Longitude (°E)	Latitude (°N)	Depth (km)	M_L	Agency
A	2017/04/05	15:43:29.00	21.7722	38.3172	14	4.5	GINOA
B	2017/01/09	10:23:02.80	21.7198	38.3480	10	3.4	GINOA
C	2017/04/05	20:45:15.60	21.7607	38.3257	6	2.6	GINOA
C	2017/04/05	20:45:15.30	21.7500	38.3213	5.5	—	This article

Event	Centroid Depth (km)	Strike (°)	Dip (°)	Rake (°)	M_w	Frequency (Hz)	Distance (km)	Method	Comment
A	6	204	47	−132	4.4	0.04–0.06	27–67	Waveforms	Reference (GINOA)
A	6 (fixed)		Figure 2		4.4	0.05–0.10	381–609	Envelopes + one polarity	This article
B	8	48	72	151	3.7	0.08–0.20	5–34	Waveforms	Reference (this article)
B	8 (fixed)		Figure 3		3.6	0.08–0.20	39–137	Envelopes + one polarity	This article
C	6	206	52	−167	2.8	0.08–0.50	8–17	Waveforms	Reference (this article)
C	6 (fixed)		Figure 4		2.8	0.5–1.5	5–46	Envelopes + two polarities	This article

GINOA, Geodynamics Institute, National Observatory of Athens.

10%, 3%, or 1%. Numerically, the threshold is the same for X, for misfit (misfit $= R/D$, in which D is the sum of squared data), or for variance reduction (VR $= 1 -$ misfit). These threshold estimates are in agreement with other authors. For example, Halló and Gallovič (2016) calculated data covariance by assuming modest variations of velocity models, and Vackář *et al.* (2017) calculated the errors from real noise; both groups arrived at results equivalent to our Thr ~ 1%–5%. On the other hand, Duputel *et al.* (2012), in their neighborhood algorithm search of source parameters, investigated normalized misfits in a broader threshold, up to Thr = 50%.

The most important features of the method can be summarized as follows:

- normalized envelope shapes, to reduce effects of imprecise velocity models and metadata errors;
- cross correlation, to help in the L2-norm fitting of envelope shapes;
- grid search, to systematically explore the parameter space of strike, dip, and rake;
- posterior renormalization, to retrieve correct scalar moment; and
- thresholding, to explore resolution and uncertainty.

The envelope-inversion method has been implemented into the ISOLA software (Sokos and Zahradník, 2013). So far, these codes have been broadly used for waveform inversion (Agurto *et al.*, 2012; Choi *et al.*, 2012; Hicks and Rietbrock, 2015; Cambaz and Mutlu, 2016; Zahradník *et al.*, 2017). Now, in the ISOLA-GUI, users can easily switch, with a single click, between the traditional waveform inversion and the new envelope inversion, while all other functions such as data preparation, Green's functions, and so on remain available. Adding or removing stations with polarity constraint and/or changing the misfit threshold is fully interactive and fast, hence user-friendly.

APPLICATION EXAMPLES

Three shallow earthquakes are presented to demonstrate the potential of full-waveform envelopes at epicentral distances which are problematic for waveform inversions. The basic parameters of the earthquakes (such as origin time, location, and local magnitude) are shown in Table 1. Reference focal mechanisms are accurate within ~10° of the source angles. We use data from seismic networks in Greece (see Data and Resources). The basic velocity model is that of Novotný *et al.* (2001; hereafter, VM1). Most calculations were also made in an alternative 1D model, VM2 (Haslinger *et al.*, 1999). Global waveform and envelope fit from all used stations is measured by VR (VR ≤ 1). Differences between focal mechanisms are quantified by the K-angle (Kagan, 1991).

Envelopes of an M_w 4.4 Earthquake Analyzed at 381–609 km

The focal mechanism solution of event A was previously reported by the Geodynamics Institute, National Observatory of Athens (GINOA), using waveform inversion. The GINOA mechanism (Table 1), representing a reference solution, was calculated from eight near-source stations, at distances of 27–67 km (Fig. 2).

Here we are interested in 12 regional stations at epicentral distances of 118–609 km, investigated with velocity model VM1, and at frequencies 0.05–0.10 Hz. Envelopes of real and synthetic seismograms are calculated in this frequency band. Attempting waveform inversion from all the 12 stations, only 3 (118–220 km) were matched well. However, using only the distant stations (381–609 km), the situation was quite different. As shown in Ⓔ Figure S1, available in the electronic supplement to this article, the waveform match was poor (VR 0.17), we obtained low magnitude M_w 4.2, and the focal mechanism was far from the reference one (K-angle 64°). The results were very similar for the two velocity models considered. All failed in explaining the real waveform data at distant stations. At frequencies < 0.05 Hz, the sensitivity to an imprecise velocity model would be weaker; however, in the present case, the low-frequency signal is hidden in noise.

On the contrary, we demonstrate that distant stations (381–609 km) at 0.05–0.10 Hz can be successfully inverted in terms of envelopes, *a posteriori* constrained with just a single clear polarity (dilatation at NVR station). As shown in Figure 2c, within a 10% misfit threshold, we obtain a well-resolved T axis, whereas the P axis is ambiguous, producing two clustered families of nodal lines. One family is close to the reference solution, featuring the minimum K-angle deviation of 7°. Moment magnitude (M_w 4.4) agrees with the reference. The best-fit solution deviates more from the reference (K-angle 39°). However, the 10% difference in the global misfit produces only small variations in the envelopes (the match improves in one station and deteriorates in another); that is, the physical meaning of the formal best-fitting mechanism is limited. For more illustrations of the usefulness of envelopes see Ⓔ Figs. S2 and S3. As opposed to Figure 2, the envelopes in Ⓔ Figure S3 are intentionally plotted without any shift between real and synthetic data. The shifts were used only to enable quantification of the shape similarity with the L2 misfit. They serve neither for correcting the velocity model nor for aligning data with theoretical Green's functions.

This example indicates that the entire family of solutions is the main result of the method, because it hopefully contains the correct solution, whereas the best-fitting solution may deviate from it. But how large should or can the threshold be when defining the family? In this case, we were successful with a relatively large (10%) threshold recommended in the Method section. The other real and synthetic examples of this article show that often we get resolution only in a narrower, less reliable threshold (3%). Thus, the usable threshold itself characterizes the quality of the solution; see also the Discussion section.

Envelopes of an M_w 3.7 Earthquake Analyzed at 39–137 km

Because of the low magnitude of event B, no routine solution exists in the moment-tensor catalog of GINOA. We studied this earthquake considering a set of 15 stations at distances 5–137 km (Fig. 3) and various subsets. The lowest available frequency range providing a good signal is 0.08–0.2 Hz. Waveforms could be well matched at the five nearest stations (5–34 km). The corresponding centroid moment tensor has been adopted as the reference solution (Table 1).

But what if the five nearest stations were absent? Could we calculate the focal mechanism then? We found that 10 distant stations (39–137 km) can be matched in terms of their envelopes, and, as shown in Figure 3c, we obtain basically the same type of mechanism as in the reference solution. A single polarity is used, and a 3% misfit threshold is analyzed. The use of this threshold (compared to 10% for event A) is dictated by the considerably less pronounced minima of the misfit function in the present case. Within the adopted ensemble of nodal lines, we found solutions as close to the reference as a K-angle of 14°. By removing the noisiest components (e.g., E at RLS and N at VLS), the agreement with the reference solution can improve even further.

Envelopes of an M_w 2.8 Earthquake Analyzed at 5–46 km

This small and thus challenging earthquake (event C) is an aftershock of event A. Seven stations were used to infer its focal mechanism (Fig. 4). At the nearest short-period station, UPR (5 km), we encountered a good signal at > 0.2 Hz. The nearest broadband stations AGRP, ROD3, and EFP (8–17 km) can be inverted at > 0.08 Hz. At the remaining three broadband stations (up to 46 km), we must employ higher frequencies > 0.5 Hz.

The experiments started with standard waveform inversion. Only the three nearest broadband stations were well matched in the lowest available frequency range of 0.08–0.5 Hz, providing a solution shown in Table 1 as the reference. For a better justification of the solution, we employed the envelope inversion at all seven available stations in a common range, 0.5–1.5 Hz, beyond the microseismic noise peak. The inversion with (various) single-polarity constraints provided two distinct families of P axes, similar to those observed for event A in Figure 2. However, applying a polarity constraint at two stations and investigating the 3% misfit threshold, the P axis is unambiguous in Figure 4c. The envelopes are matched well, and the agreement with the reference solution is good. The 3%-misfit ensemble in Figure 4 is relatively compact, and it contains solutions deviating from the reference mechanism by K-angles < 20°. In this sense, we confirm the focal mechanism estimate previously obtained by a three-station waveform inversion and conclude that it is similar to that of the mainshock.

DISCUSSION

Events A and B demonstrated the usefulness of envelopes in the simulated absence of near-source stations, when waveforms at distant regional stations cannot be matched due to imperfect velocity models. Event C demonstrated how to increase the reliability of the mechanism found from very few near-source stations using envelopes at the nearby and more-distant stations.

It should be noted that one station used for event B had a completely wrong gain, and one station used for event C had a flipped sign for the N and E components. None of these

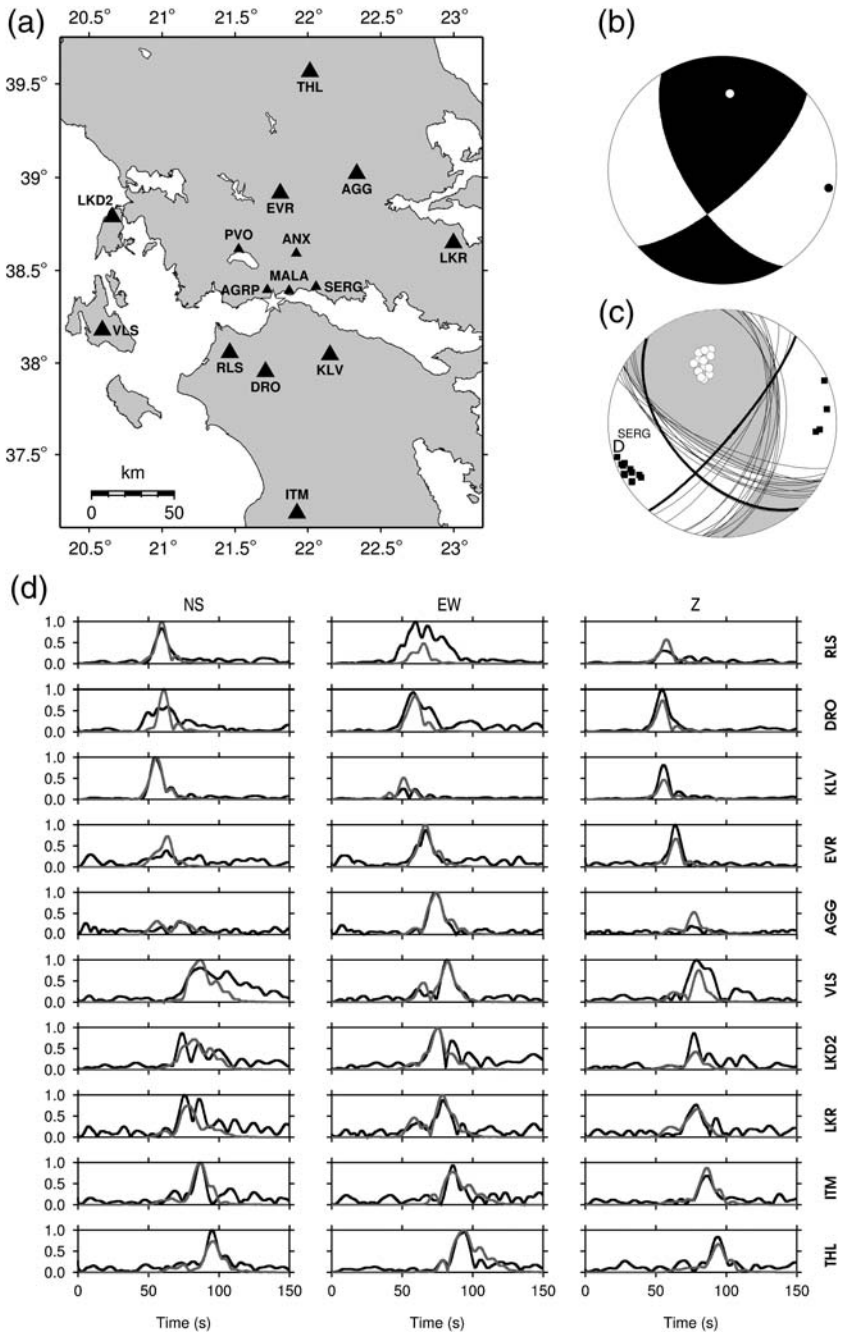

▲ **Figure 3.** Event B, M_w 3.7. (a) Two groups of stations are distinguished: 5 near-source stations (5–34 km), shown as small symbols, and 10 more distant stations (39–137 km), shown as large symbols. The star shows the epicenter. (b) Focal mechanism by standard waveform inversion applied to the near-source stations, that is, the reference solution. (c) Envelope inversion at the distant stations (39–137 km), where the standard waveform inversion fails. A single polarity constraint (station SERG, D = down) is used. Shown by shading in (c) is the best-fitting envelope solution. Nodal lines correspond to the 3% misfit threshold; the bold one is the nearest to the reference. The envelope-inverted mechanism, not using any near-source station, is in agreement with the reference mechanism. (d) The observed (black) and synthetic (gray) envelopes, 0.08–0.20 Hz; VR = 0.62.

problems, generally serious for waveform methods, affected the envelope inversion.

The lowest available frequencies were used throughout this article, that is, the frequencies at which the signal reasonably exceeds the noise, and they are recommended. The suitable ranges depend on magnitude and epicentral distance. For events A, B, and C, we resolved focal mechanisms in the 0.05–0.10, the 0.08–0.20, and the 0.5–1.5 Hz ranges, respectively. Low frequencies were at our disposal for event A, thanks to the relatively large distances with well-developed *Lg* waves and thanks to the relatively large magnitude (M_w 4.4). The ensemble of nodal lines featured small scatter, even at the relatively large 10% misfit threshold. An unsuccessful attempt to extend the frequency range for event B to 0.08–0.40 Hz was demonstrated in Ⓔ Figure S4; we observed loss of resolution due to microseismic noise. In that case, a small scatter of nodal lines was detected only in a very narrow threshold (1%), for which physical reliability is very limited, and thus should be considered as a failure of the method. The high-frequency inversion of the smallest earthquake, event C (M_w 2.9), was possible because the 0.5–1.5 Hz range is basically above the microseismic noise, and these high-frequency envelopes could be modeled in a simple crustal model, thanks to the short epicentral distances.

Standard waveform inversions at regional stations usually fail at frequencies and epicentral distances > 10 MSW. For event A, we demonstrated the applicability of the envelope inversion up to ~13–20 MSW. For event B, the waveform inversion was feasible at less than 3 MSW; that is because the used frequency range was close to the microseismic noise peak. Nevertheless, the envelopes extended the inversion capability up to 9 MSW. The envelope inversion of event C appears to be possible even up to 23 MSW. We believe that such an extension of the applicability range, relative to waveforms, is encouraging.

The minimal posterior polarity constraints (one or two polarities only) were intentionally applied to events A–C, simply to overcome the insensitivity of envelopes with respect to the 180° ambiguity of rake. Ⓔ Figure S5 explains how the polarity constraint works. Naturally, and mainly when grid-search solutions are strongly nonunique, additional polarities should be employed. As in any method making use of polarities, only clear impulsive onsets should be used. Moreover, it is useful to check the consistency of polarities on the three recorded com-

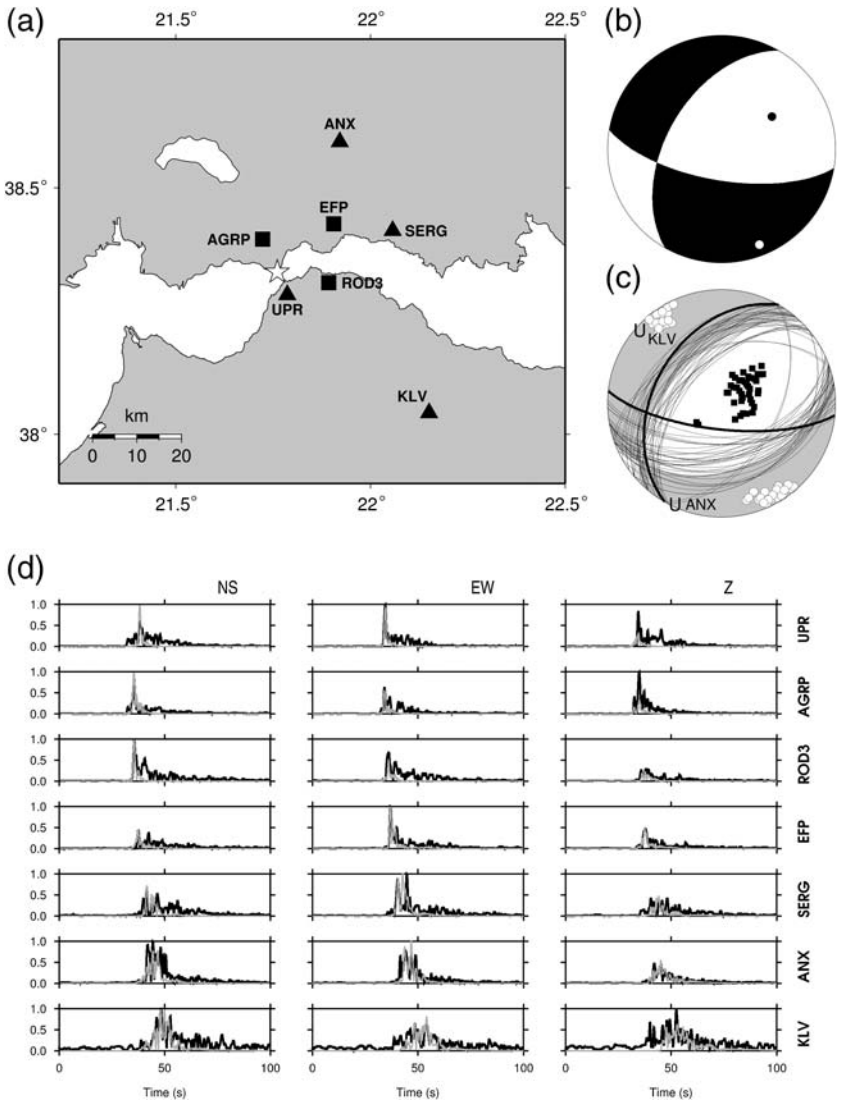

▲ **Figure 4.** Event C, M_w 2.8. (a) The seven stations considered in the focal mechanism inversion (5–46 km). Three nearest broadband stations (8–17 km) are shown by squares. A star shows the epicenter. (b) The focal mechanism, calculated by waveform inversion from the stations shown by squares, represents the reference solution. (c) The focal mechanism calculated by envelope inversion from all stations. The best-fitting envelope solution is shown by shading in (c). Nodal lines correspond to the 3% misfit threshold of the solutions constrained with two polarities (Stations KLV and ANX, U denotes up); shown in bold are nodal lines closest to the reference. The envelope technique improved justification of the three-station waveform solution. (d) The observed (black) and synthetic (gray) envelopes, 0.5–1.5 Hz; VR = 0.52.

ponents with the station azimuths. Here, we remind the reader that, as explained in the Method section, the envelope inversion can also be applied with a prior polarity constraint (as in the cyclic scanning of the polarity solutions [CSPS] method of Fojtíková and Zahradník, 2014).

To further clarify the effects of velocity models, frequency ranges, and noise, a series of synthetic tests was performed (Ⓔ Figs. S6–S10). Similar to real-data applications, the tests proved that envelopes can be more robust than waveforms, with respect to imprecise velocity models. This is especially true if the noise is low, and real envelope shapes differ from the shapes in theoretical velocity models mainly by time shifts. Because the real models are not known, the success of the envelopes cannot be *a priori* guaranteed. The best-fit solution can be biased relative to the true solution and, therefore, it is essential to adopt solutions in a reasonable threshold above the minimum misfit.

In the Method section, we arrived at recommended misfit thresholds of ~1%–10%, and in the synthetic tests we confirmed the suitability of this option by studying the analogy with waveform-inversion uncertainties. If adopting grid-search solutions having a misfit within the 10% range from the best-fit solutions, it is more likely that the true solution is among them. In our opinion, envelope inversions are best justified when nodal lines form a compact ensemble in the 10% (or higher) misfit threshold. However, in the safe 10% range, the solution might be sometimes strongly nonunique, perhaps even losing any resolution. On the contrary, it is easy to obtain an apparently well-resolved solution (low scatter of nodal lines) in the 3% range, but the cost we pay for the resolution is a risk that the true solution may not lie in the ensemble. Our current opinion is that, if the solution seems to be resolved only in the 1% risky misfit range, which is the case of shallow misfit minima, the user should consider the method has failed. Naturally, any solutions characterized by low VR, typically VR < 0.5 (misfit > 0.5), are always doubtful.

We observed in real data, as well as in the synthetic tests, that the misfit variation with the trial source depth is weak. We can say that, contrary to waveform inversions, the envelopes may not resolve focal depth. We recommend that the user applies the method, using a hypocenter location as accurate as possible, and checks the solutions also at nearby depths. If the retrieved focal mechanism ensembles at nearby depths differ from each other, then the method has failed. On the other hand, in all investigated real and synthetic data sets, the envelope inversion provided very good estimates of the scalar moment (hence also a reliable moment magnitude).

CONCLUSION

The envelope-inversion method has been proposed in this article for estimating focal mechanisms and moment magnitudes of shallow crustal earthquakes analyzed from poor data sets (e.g., at epicentral distances large compared to the wavelength

and using imprecise velocity models). The envelope inversion is not meant to substitute the waveform inversion, if the latter works well. For example, deeper events (not tested in this article) are less affected by complex shallow crustal structures; thus such events might not need the envelope technique.

We presented three convincing real-data examples, supported by synthetic tests in the Ⓔ electronic supplement. These demonstrated the pros and cons of the method when applied to shallow crustal earthquakes at local to near-regional distances. The envelope inversion appears to be less sensitive to inaccuracies in the velocity model than the waveform inversion. This is definitely an advantage, because if waveform inversion fails, envelopes might provide an estimate of the focal mechanism. Obviously, there are some limits; thus noisy data as well as very inaccurate velocity models would provide false mechanisms, even in the case of envelope inversion. Moreover, the method does not resolve focal depth. However, at least in the tests performed so far, the envelope method appears to be applicable up to ~20 MSW; this is a significant extension compared to waveforms, which are usually limited to ~10 MSW. Moreover, envelopes provide a good estimate of moment magnitude.

Envelopes represent a simplification compared to waveforms. As such, the resulting focal mechanisms have limited precision and resolution, and the best-fit solution should not be considered as the main result. The result is an ensemble of solutions, within a reasonable threshold below the largest VR (above the minimal misfit). If the ensemble is compact (not very dispersed), then a mean moment tensor could be a proper representation of the result. Two methods (the chi-square statistic and comparisons with analytical uncertainty assessment of waveforms) were used to show that reasonable thresholds in the investigated type of problems are ~10% or 3%. The 10% threshold is safe, but solutions in this range are often highly nonunique, thus losing resolution. The 1% range will almost always have a better resolution, but is very risky. In this sense, the usable threshold (allowing resolution) is itself an indicator of the solution quality, the higher the usable threshold, the better.

The main risk is that this new tool always provides a solution, but this solution may sometimes be misleading. Similar to waveform inversions, even apparently well-fitted data (typically with VR > 0.5) might provide false mechanisms, due to a number of reasons, as explained above. This is why any additional check of the resulting focal mechanisms is useful, for example, a comparison with solutions based on many polarities. It is almost mandatory to perform repeated inversions with alternative velocity models and with several alternative frequency bands. We emphasize that the envelope inversion of a rare (hence important) event in a sparse network is a research task rather than a routine task. The ISOLA software is a user-friendly environment that can be used to deeply investigate such events.

DATA AND RESOURCES

Seismic waveforms used in this study are freely available at http://eida.gein.noa.gr/ (last accessed December 2017) and http://seismology.resif.fr (last accessed August 2017). The plots were made using the Generic Mapping Tools v.4.2.1 (http://www.soest.hawaii.edu/gmt/, last accessed December 2017). Software ISOLA (Sokos and Zahradník, 2013) can be downloaded from https://github.com/esokos/isola (last accessed December 2017) and with the latest updates from http://geo.mff.cuni.cz/~jz/for_Costa_Rica/ (last accessed December 2017). ⊠

ACKNOWLEDGMENTS

The authors acknowledge access to seismic waveform data of the following seismic networks: Hellenic Seismic Network, doi: 10.7914/SN/HL; the University of Patras, Seismological Laboratory, doi: 10.7914/SN/HP (some stations cooperated with Charles University, Prague, Czech Republic); the Seismological Network of the Aristotle University of Thessaloniki, doi: 10.7914/SN/HT; and the Corinth Rift Laboratory Network, doi: 10.15778/RESIF.CL. E. S. acknowledges financial support by the HELPOS Project, "Hellenic Plate Observing System" (MIS 5002697), and J. Z. was supported by CzechGeo/EPOS (LM2015079). The authors thank Olga-Joan Ktenidou for checking the English in the article. The editors and two anonymous reviewers considerably helped improve the article.

REFERENCES

Agurto, H., A. Rietbrock, I. Ryder, and M. Miller (2012). Seismic-afterslip characterization of the 2010 M_w 8.8 Maule, Chile, earthquake based on moment tensor inversion, *Geophys. Res. Lett.* **39,** 1–6, doi: 10.1029/2012GL053434.

Baker, T., R. Granat, and R. W. Clayton (2005). Real-time earthquake location using Kirchhoff reconstruction, *Bull. Seismol. Soc. Am.* **95,** 699–707, doi: 10.1785/0120040123.

Boore, D. (1983). Stochastic simulation of high-frequency ground motions based on seismological models of the radiated spectra, *Bull. Seismol. Soc. Am.* **73,** 1865–1894.

Cambaz, M. D., and A. K. Mutlu (2016). Regional moment tensor inversion for earthquakes in Turkey and its surroundings: 2008–2015, *Seismol. Res. Lett.* **87,** 1082–1090.

Cesca, S., S. Heimann, and T. Dahm (2010). Rapid directivity detection by azimuthal amplitude spectra inversion, *J. Seismol.* **15,** 147–164, doi: 10.1007/s10950-010-9217-4.

Choi, H., T. K. Hong, X. He, and C. E. Baag (2012). Seismic evidence for reverse activation of a paleo-rifting system in the East Sea (Sea of Japan), *Tectonophysics* **572/573,** 123–133, doi: 10.1016/j.tecto.2011.12.023.

Chouet, B. (1979). Temporal variation in the attenuation of earthquake coda near Stone Canyon, California, *Geophys. Res. Lett.* **6,** 143–146, doi: 10.1029/GL006i003p00143.

Dahal, N. R., and J. E. Ebel (2016). Nonlinear moment tensor inversion of the envelopes and cumulative energy of regional seismic waveforms, *88th Annu. Meet. East. Sect. Seismol. Soc. Am*, Reston, Virginia, 23–26 October 2016.

Dias, F., J. Zahradník, and M. Assumpção (2016). Path-specific, dispersion-based velocity models and moment tensors of moderate events recorded at few distant stations: Examples from Brazil and Greece, *J. South Am. Earth Sci.* **71,** 344–358, doi: 10.1016/j.jsames.2016.07.004.

Duputel, Z., H. Kanamori, V. C. Tsai, L. Rivera, L. Meng, J. P. Ampuero, and J. M. Stock (2012). The 2012 Sumatra great earthquake sequence, *Earth Planet. Sci. Lett.* **351/352,** 247–257, doi: 10.1016/j.epsl.2012.07.017.

Fojtíková, L., and J. Zahradník (2014). A new strategy for weak events in sparse networks: The first-motion polarity solutions constrained by single-station waveform inversion, *Seismol. Res. Lett.* **85,** 1265–1274, doi: 10.1785/0220140072.

Halló, M., and F. Gallovič (2016). Fast and cheap approximation of Green functions uncertainty for waveform-based earthquake source inversions, *Geophys. J. Int.* **207,** 1012–1029, doi: 10.1093/gji/ggw320.

Hardebeck, J. L., and P. M. Shearer (2003). Using *S*/*P* amplitude ratios to constrain the focal mechanisms of small earthquakes, *Bull. Seismol. Soc. Am.* **93,** 2434–2444, doi: 10.1785/0120020236.

Haslinger, F., E. Kissling, J. Ansorge, D. Hatzfeld, E. Papadimitriou, V. Karakostas, K. Makropoulos, H. G. Kahle, and Y. Peter (1999). 3D crustal structure from local earthquake tomography around the Gulf of Arta (Ionian region, NW Greece), *Tectonophysics* **304,** 201–218, doi: 10.1016/S0040-1951(98)00298-4.

Hicks, S. P., and A. Rietbrock (2015). Seismic slip on an upper-plate normal fault during a large subduction megathrust rupture, *Nat. Geosci.* **8,** 955–960, doi: 10.1038/ngeo2585.

Kagan, Y. Y. (1991). 3-D rotation of double-couple earthquake sources, *Geophys. J. Int.* **106,** 709–716, doi: 10.1111/j.1365-246X.1991.tb06343.x.

Novotný, O., J. Zahradník, and G. A. Tselentis (2001). Northwestern Turkey earthquakes and the crustal structure inferred from surface waves observed in Western Greece, *Bull. Seismol. Soc. Am.* **91,** 875–879, doi: 10.1785/0120000116.

Sokos, E., and J. Zahradník (2013). Evaluating centroid-moment-tensor uncertainty in the new version of ISOLA software, *Seismol. Res. Lett.* **84,** 656–665, doi: 10.1785/0220130002.

Tan, Y., and D. Helmberger (2007). A new method for determining small earthquake source parameters using short-period *P* waves, *Bull. Seismol. Soc. Am.* **97,** 1176–1195, doi: 10.1785/0120060251.

Vackář, J., J. Burjánek, F. Gallovič, J. Zahradník, and J. Clinton (2017). Bayesian ISOLA: New tool for automated centroid moment tensor inversion, *Geophys. J. Int.* **210,** 693–705, doi: 10.1093/gji/ggx158.

Vavryčuk, V., and S. G. Kim (2014). Nonisotropic radiation of the 2013 North Korean nuclear explosion, *Geophys. Res. Lett.* **41,** 7048–7056, doi: 10.1002/2014GL061265.

Wéber, Z. (2006). Probabilistic local waveform inversion for moment tensor and hypocentral location, *Geophys. J. Int.* **165,** 607–621, doi: 10.1111/j.1365-246X.2006.02934.x.

Zahradník, J., and F. Gallovič (2010). Toward understanding slip inversion uncertainty and artifacts, *J. Geophys. Res.* **115,** no. B09310, doi: 10.1029/2010JB007414.

Zahradník, J., H. Čížková, C. R. Bina, E. Sokos, J. Janský, H. Tavera, and J. Carvalho (2017). A recent deep earthquake doublet in light of long-term evolution of Nazca subduction, *Sci. Rep.* **7,** no. 45153, doi: 10.1038/srep45153.

Zahradník, J., J. Janský, and K. Papatsimpa (2001). Focal mechanisms of weak earthquakes from amplitude spectra and polarities, *Pure Appl. Geophys.* **158,** 647–665, doi: 10.1007/PL00001198.

Jiří Zahradník
Charles University
Faculty of Mathematics and Physics
V Holešovičkách 2
180 00 Prague 8
Prague, Czech Republic
jz@karel.troja.mff.cuni.cz

Efthimios Sokos
Department of Geology
Seismological Laboratory
University of Patras
26504 Rio
Patras, Greece
esokos@upatras.gr

Published Online 28 February 2018